AIMS Materials Science, 13(5): 1068–1094.
DOI: 10.3934/matersci.2026050
Received: 06 August 2026
Revised: 21 October 2026
Accepted: 03 November 2026
Published: 19 November 2026

https://www.aimspress.com/journal/Materials

Research article

Phase structure and specific features of polylactide and ethylene-vinyl acetate copolymer blends

Leonid Vayshbeyn[1,2,*], Elena Mastalygina[1,2], Bekzod Khaydarov[2,3], Aleksey Krivandin[4] and Anatoly Popov[1,2]

[1] Laboratory of Physics-Chemistry of Synthetic and Natural Polymers Compositions, Emanuel Institute of Biochemical Physics, Russian Academy of Sciences, 4 Kosygin St, Moscow 119991, Russia
[2] Scientific Laboratory «Advanced Composite Materials and Technologies», Plekhanov Russian University of Economics, 36 Stremyanny Ln, Moscow 117997, Russia
[3] Department of Functional Nanosystems and High-Temperature Materials, National University of Science & Technology «MISIS», 4 Leninsky Pr, Moscow 119049, Russia
[4] Center of X-ray diffraction analysis, Emanuel Institute of Biochemical Physics, Russian Academy of Sciences, 4 Kosygin St, Moscow 119991, Russia

* **Correspondence:** Email: dz1376@mail.ru.

Abstract: Developing binary polymer blends makes it possible to obtain materials with a combination of characteristics of the original components, often surpassing the properties of each polymer individually. The aim of this work was to study the morphological features of blends of polylactic acid (PLA) and ethylene-vinyl acetate copolymer (EVA) with 28 wt.% of vinyl acetate-units, as well as to identify compositions with abnormal physical and mechanical properties. By means of scanning electron microscopy (SEM) and Fourier-transform infrared spectroscopy (FTIR), it was identified that the blends with more than 30 wt.% and less than 60 wt.% of PLA had co-continuous morphology. It was shown that, for blends with a PLA content of more than 40 wt.%, PLA predominates on the surface of the films, which can be explained by the lower viscosity of the PLA melt compared to the EVA melt. Polymer phase interaction zones, signs of hydrogen bonds formation, and a negative deviation of the density parameter from additivity were found for blends with a lower PLA content (20–50 wt.%). This could affect the properties of the materials and lead to a non-additive dependence of physical and mechanical characteristics on the composition of these blends (for instance, tensile strength and elongation at break). For the PLA-rich blends, even

adding 5 wt.% of EVA to PLA significantly worsened the mechanical properties of the latter. According to differential scanning calorimetry (DSC), the process of PLA crystallization took place in the presence of molten liquid EVA, which can act as a plasticizer for PLA, contributing to the improvement of crystallites. In the future, the ability of PLA/EVA blends to degrade under the influence of various factors will be comprehensively studied.

Keywords: polymer blends; polylactic acid; ethylene-vinyl acetate copolymer; phase structure; structure-property relationships; mechanical properties; thermophysical behavior

1. Introduction

Plastics based on traditional synthetic polymers, widely used for packaging and agriculture, are characterized by high resistance to degradation under environmental conditions. As a result, the problem of accumulation of polymer waste has become urgent. One of the most promising approaches to solving this environmental problem is the use of biodegradable polymers, including those from renewable raw materials, for products with a short life cycle [1]. Poly(lactide) or poly(lactic acid) (PLA) is the most widespread and high-tonnage biodegradable polymer. This polymer is obtained from renewable raw materials and is characterized by biodegradability in industrial compost conditions (elevated temperatures and target microbiota) [2]. In addition, its technological properties are similar to traditional plastic, such as polyethylene terephthalate (PET). PLA is a promising material for fused deposition modeling (FDM technology) [3], presenting good mechanical properties—in particular, high tensile strength and Young's modulus—as well as good bending strength, higher than those of polystyrene, polypropylene, polyethylene, or other polymers [4]. However, PLA is characterized by high brittleness and low impact strength, and its elongation at break is less than 10%, which limits its use in applications where plastic deformation under high loads is required. PLA is also resistant to abiotic environmental factors (for example, oxidation under the influence of oxygen in the air) and has limited biodegradability under the influence of microbiota as a result of being in a glassy state at operating temperature [5].

To regulate the abovementioned disadvantages of PLA, blends with modifying low- and high-molecular weight additives have been created. M. Puthumana et al. reviewed different methods to modify PLA [6]; for example, copolymerization with glycolic acid was applied to increase the crystallinity of PLA, making it more suitable for medical applications. According to another approach, PLA copolymerization with poly(trimethylene carbonate) improved its ductility, decreased brittleness, and increased melting temperature. The review by Y. Cheng et al. stated that blending PLA with trimethylsilyl could significantly improve hydrophilicity and cell affinity [7]. Also, chitosan seems to be a promising substance for copolymerization with PLA for better adsorption and adhesion to living cells [8]. S. Deng et al. developed blends of PLA with different elastomers by reactive melt blending. As a result, the main problems of PLA (inferior melt stability and inherent brittleness) were fixed, and melt stability of PLA was achieved, which is crucial for 3D printing and extrusion [9]. A. Olkhov et al. used ozonide of oleic acid triglyceride (1–5 wt.%) as a plasticization additive for PLA, resulting in an increase in relative elongation at break of PLA (3 wt.% of ozonide was the most effective) [10].

In this work, blends of PLA with an ethylene-vinyl acetate copolymer (EVA) in a wide range of compositions have been studied. A comprehensive literature review on the topic of PLA/EVA blends has shown the presence of only fragmentary data on the structure and properties of such materials. Most researchers have studied the effect of vinyl acetate units in EVA copolymer on the properties of PLA/EVA blends at a certain EVA content from the blend (usually 20% by weight). P. Ma et al. investigated the blend 80PLA/20EVA with different vinyl acetate (VA) content in an EVA copolymer [11]. It was shown that when adding 20 wt.% EVA to PLA, the elongation at break increased sharply to more than 300%, while the yield strength decreased compared to neat PLA. Compatibility between PLA and EVA improved with increasing VA content. The strength at break for the 80PLA/20EVA blends initially increased at a VA content of up to 50 wt.% and then decreased due to the weak interfacial adhesion between PLA and EVA. P. Xu et al. also studied 80PLA/20EVA blends as blown films, which showed better impact strength and tensile strength compared to PLA films, while maintaining high transparency. The EVA with 80 wt.% VA units showed a better modification effect on PLA than the EVA with 60 wt.% VA units. For example, elongation at break of 220% and a tensile strength of 60 kN/m were achieved in tensile tests [12].

D. Kugimoto et al. identified that different contents of vinyl acetate units (20, 50, 80 wt.% of VA in EVA) also affected the light transmission of films based on PLA/EVA blends [13]. The small size of the dispersed particles also helped to reduce light scattering. In conclusion, the addition of EVA with 80 wt.% of VA units greatly improves the mechanical toughness of PLA without sacrificing its optical transparency. In continuation of this work, D. Kugimoto showed that the addition of EVA increased the elasticity of the PLA melt, regardless of the VA content, even if EVA is in the dispersed phase [14].

N. Karimpour-Motlagh et al. studied the selective permeability of PLA/EVA blends. It was concluded that the system with 75–100 wt.% PLA demonstrated significantly lower permeability than the system with a 75–100 wt.% EVA. The analysis of the selectivity parameter showed the lowest permeability to O_2 and the highest selectivity for CO_2/N_2 and O_2/N_2, which was favorable for use in food packaging. Additionally, the blend with a high PLA content was slightly more sensitive to relative humidity compared to the blends with a high EVA content due to the more hydrophilic nature of PLA [15].

N. Ishaque et al. studied PLA/EVA blends with 20, 30, 50 and 70 wt.% of EVA with addition of 30% aspirin. Blending PLA with EVA improved elongation at break and decreased brittleness. Also, adding EVA increased the temperature stability of PLA until 300 °C [16]. D.H. Han et al. studied blends with a PLA content from 0 to 40 wt.%. With the increase in PLA in the EVA matrix, tensile strength and modulus of elasticity increased, while elongation at break decreased, which can be explained by the dispersion of the rigid PLA in the EVA matrix [17]. T. Tábi researched blends of PLA with EVA contents of 2, 5, 10, 15, and 20 wt.%. It was shown that PLA crystallinity increased from 19% for neat PLA to a maximum of 40% for the blend of 95PLA/5EVA. Also, there was a connection between impact strength, annealing temperature, and different crystal forms of PLA. With increasing annealing temperature, impact strength was increased [18].

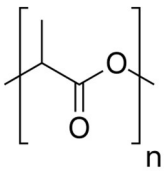
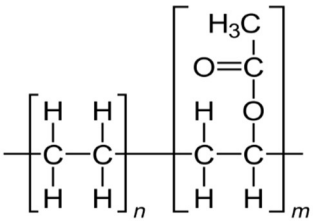
The main purpose of this work was to study morphological features and establish ranges of phase transitions of blends of PLA and EVA with 28 wt.% of VA units, as well as to identify compositions with abnormal physical and mechanical properties. In the future, the ability of PLA/EVA blends to degrade under the influence of various factors will be comprehensively studied.

2. Materials and methods

2.1. Materials

This investigation used film materials based on PLA, EVA with a vinyl acetate content of 28 wt.%, and their blends. The main characteristics of the polymers are given in Table 1.

Table 1. Characteristics of the applied PLA and EVA according to technical data sheets and scientific studies.

Polymer	PLA	EVA
Producer	NatureWorks (USA)	LG Chem (Korea)
Trademark	PLA 4043D	EVA 28005
Density	1.22 g/cm^3	0.951 g/cm^3
Molecular weight (M_w)	10–15 × 10^4 Da [19]	7–8 × 10^4 Da [20]
Melt flow index (MFI)	6 g/10 min (210 °C, 2.16 kg)	5 g/10 min (190 °C, 2.16 kg)
Onset melting temperature	140–150 °C	74 °C
Relative elongation at break	7% (ASTM D882, tensile rate of 50 mm/min)	700% (ASTM D638, tensile rate of 500 mm/min)
Structural formula		

The blends were obtained in a wide range of compositions with PLA contents of 5, 10, 20, 30, 40, 50, 60, 70, 80, 90, and 95 wt.%. Individual polymers (neat PLA and EVA) were subjected to similar processing conditions as the blends. Table 2 shows the compositions of the obtained materials. The volume composition of PLA/EVA blends was calculated according to the polymer densities. For obtaining the blends, the polymers were mixed in a melt by a two-rotor laboratory mixer (Brabender Plasticorder, Germany) at 170 ± 3 °C for 7 min with a rotation speed of 100 rpm. Then, materials were cooled, crushed to a fraction of 0.5 cm, and pressed to films by a PRG-10 hydraulic press (LabTools LLC, Russia) at 175 ± 3 °C followed by quenching in water at 22 ± 2 °C. Film materials with a thickness of 120 ± 20 μm were based on neat PLA and EVA, as their blends were subjected to further study.

Table 2. Compositions of the materials under investigation.

Weight content of PLA in the PLA/EVA blend, wt.%	100	95	90	80	70	60	50	40	30	20	10	5	0
Volume content of PLA in the PLA/EVA blend, vol.%	100	93.6	87.5	75.7	64.5	53.9	43.8	34.2	25.0	16.3	7.9	3.9	0

2.2. Methods

2.2.1. Scanning electron microscopy (SEM)

To study the bulk surface of the materials, SEM analysis was conducted using a Tescan Vega 3 microscope (Tescan, Czech Republic) equipped with a tungsten cathode. The chips of the film samples were obtained in liquid nitrogen. Then, samples were coated with a 15-nm gold layer by spraying at 4 mA for 4 min. The accelerating voltage was 20 kV, and the working distance was 15 mm (Jeol JFC-1600, Tokyo, Japan). The study was carried out using the secondary electron (SE) method at magnifications of 100×, 500×, 1000×, 2000×, and 20000×. ImageJ was used for processing domain sizes of the minor phase of the blend.

2.2.2. Microscopy of coherent Raman scattering of light (Raman microscopy)

Raman microscopy was used to identify the chemical composition of the phases in the bulk of the material. The spectra were obtained using a DXR3 Raman microscope (Thermo Fisher Scientific, USA) with a green 532 nm laser. The film chips obtained in liquid nitrogen were analyzed according to ISO 6775:2024 [21]. Measurements were conducted with the laser power set to 10 mW.

2.2.3. Fourier-transform infrared spectroscopy (FTIR)

FTIR was used to analyze the distribution of polymers in the near-surface layers of films. FTIR was performed on a spectrometer Lumos (Bruker, Germany) using a macromodule using the method of attenuated total reflectance (ATR platinum Diamond crystal). The scanning was performed in the range of 650–4000 cm^{-1} at a temperature of 23 ± 2 °C according to ISO 10640:2011 [22]. At a wavenumber of 3000 cm^{-1}, the radiation penetration depth is 0.67 μm; at 1700 cm^{-1}, it increases to 1.18 μm; and at 1000 cm^{-1}, it reaches 2.01 μm. Therefore, this technique allows for the assessment of the chemical composition only within a near-surface layer of up to 2 μm. To analyze the volume of the material, Raman microscopy and SEM of the samples' cross-sections were used. Spectra were processed using Bruker OPUS software (Germany).

2.2.4. Differential scanning calorimetry (DSC)

The thermophysical properties of polymers were analyzed by a differential scanning calorimetry using a DSC 214 Polyma (Netzsch, Germany). The analysis was carried out according to ISO 11357-1:2023 [23] using Concavus aluminum pans at a heating/cooling rate of 10 °C/min. The temperature scanning program was as follows: 30…200 °C (first heating), 200…30 °C (cooling), 30…200 °C (second heating). The sample weight was 10 ± 1 mg. The thermograms were processed using the Proteus NETZSCH software.

2.2.5. Wide-angle X-ray diffraction (WAXD)

The X-ray diffraction study of PLA, EVA, and PLA/EVA blend films was carried out in the Emanuel Institute of Biochemical Physics of Russian Academy of Sciences. X-ray diffraction

patterns were recorded at ambient room temperature (~25 °C) in transmission geometry on a diffractometer of local design supplied with the optical focusing of the X-ray beam and a linear position-sensitive X-ray detector (Cu X-ray tube, Ni β-filter) [24,25]. The cross-section of the X-ray beam in the plane of the sample was ~4 × 0.15 mm^2, and the distance between the sample and the detector was ~92 mm. In order to diminish instrumental smearing of diffraction lines, the X-ray detector was installed with an inclination of ~20° toward the sample holder, and the width of the detector window was limited to 4 mm by the slit overlay. Diffraction lines of polycrystalline corundum and poly(3-hydroxybutyrate) were used for calibration of the detector. X-ray diffraction intensity was corrected for X-ray absorption in the samples, background scattering, and variance in samples mass. For some films, X-ray diffraction patterns were also recorded in Bragg-Brentano geometry on a HZG4 diffractometer (Freiberger Prazisionsmechanik, Germany) with a diffracted beam graphite monochromator using a low-background polished monocrystalline silicic substrate (Cu-Kα radiation, λ = 0.1542 nm).

2.2.6. Tensile testing

Tensile testing was performed by a universal testing machine GP UG 5 DLC-0.5 (Devotrans, Turkey). Tests were carried out for the samples of type 3 (strips of 60 × 10 mm) with a tensile rate of 5 mm/min according to ISO 527-1:2019 [26], followed by determining the yield and maximum strength, elongation at break, and Young's modulus. Prior to mechanical testing, the specimens were conditioned at a temperature of 50 ± 2 °C for 2 h in a vacuum oven. The number of replicates for each sample was at least 5.

2.2.7. MFI

The MFI of the blends was calculated by the MFI tester (SNTF-Lab, China). Before the experiment, the prepared PLA/EVA blends and neat polymers were grinded and dried for 60 min at a vacuum drying chamber (Stegler VAC-52, China). The measurements were performed at 170 ± 1 °C with a weight of 1.23 or 2.16 kg according to ISO 1133-1:2022 [27]. The number of replicates for each sample was at least 7.

2.2.8. Density

Density of the samples was measured by hydrostatic weighing in distilled water by an analytical balance (AND GR-200, Japan). The analysis was performed at 23 ± 2 °C in distilled water (density of water = 0.99757 g/cm^3) according to ISO 1183-1:2019 [28]. The number of replicates for each sample was at least 5.

3. Results and discussion

The complex properties of polymer blends is largely determined not only by the chemical nature of the polymers being mixed but also by the supramolecular structure of the polymer phases themselves, the peculiarities of the polymer phase distribution, and the interaction at the interface. Many studies have shown that most polymer blends are immiscible and phase-separate due to their

large molecular weight and, consequently, low mixing entropy [29]. However, when combining two polymers of different nature in a material, it is possible to achieve new, specific properties that combine the characteristics of the individual polymers. This process can be used to improve properties such as mechanical strength, elasticity, and thermal performance, allowing for a more cost-effective development of materials compared to synthesizing entirely new polymers [30].

The blends of PLA and EVA are immiscible. During compounding in melt and subsequent cooling, the polymer phases separate, forming different types of phase structure depending on the ratio of polymers in the blend. SEM was used to study the type of phase structure being formed and the nature of polymer interaction at the phase interface. Figure 1 shows the images of the film material chips (cross-sections) of different compositions of the blends. The materials of blends with 5–30 and 60–95 wt.% PLA were characterized by a drop-matrix morphology, where the lower-content polymer was distributed as ellipsoidal domains in a continuous matrix of higher content. The blend with 20 wt.% PLA had well-differentiated PLA domains with an average particle size of 4 μm. The average domains size for the blend with 80 wt.% PLA was approximately 6.6 μm. The average domain sizes of the discontinuous phase of the PLA/EVA blends are given in Table 3.

The blends with more than 30 wt.% and less than 60 wt.% PLA had mixed co-continuous morphology, creating a material structure with a predominantly co-continuous morphology, and a drop-matrix morphology in the center of the film. This depended on differences in composition between the surface layer and the bulk. These compositions were also characterized by the planar orientation of the phases, which was most likely due to the method of producing films by hot pressing.

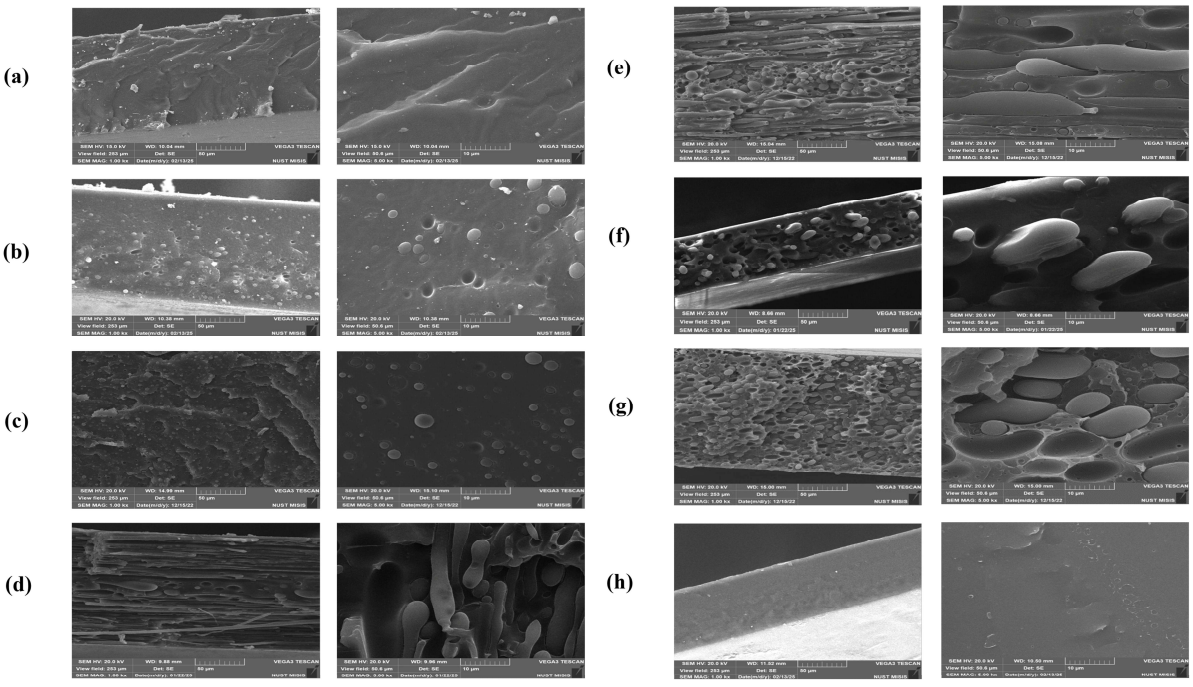


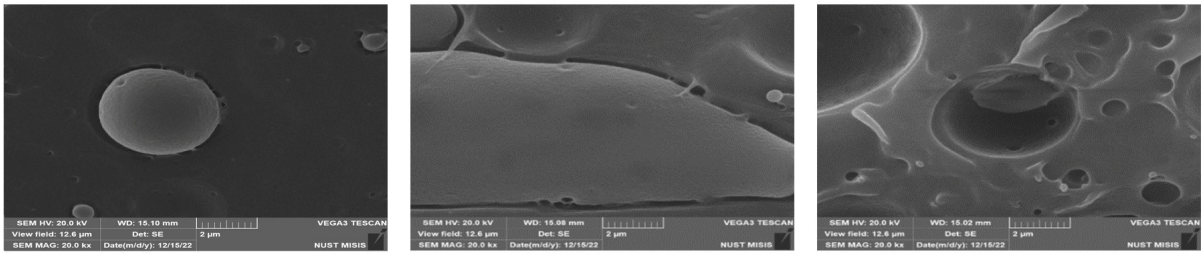
Figure 1. SEM images of cross-sections of the film samples based on PLA/EVA blends at magnifications of 1000× and 5000×. (a) Neat EVA; (b) 10PLA/90EVA; (c) 20PLA/80EVA; (d) 40PLA/60EVA; (e) 50PLA/50EVA; (f) 70PLA/30EVA; (g) 80PLA/20EVA; and (h) neat PLA (wt.%).

Table 3. Average domain size of the discontinuous phase of PLA/EVA blends.

PLA content in PLA/EVA blend, wt.%	Domain size, μm	Polymer in domains (discontinuous phase)
5	2.0 ± 0.5	PLA
10	2.0 ± 0.5	PLA
20	4.0 ± 0.5	PLA
30	4.5 ± 0.5	PLA
40	-	n.d.
50	-	n.d.
60	14.0 ± 2	EVA
70	7.5 ± 0.5	EVA
80	6.6 ± 0.5	EVA
90	7.0 ± 1	EVA
95	5.5 ± 1	EVA

Note: n.d.: non-determined because both polymer phases are continuous.

Figure 2 shows the interaction region of the PLA and EVA phases. Polymer phase interaction zones were found for blends with a lower PLA content; this could affect the properties of the materials and lead to the non-additive dependence of the characteristics on the composition of the blends. On the contrary, blends with high PLA content were characterized by poor polymer interaction at the interface with the stratification zones. S. Moradi et al. showed similar patterns: the 75PLA/25EVA blend demonstrated a matrix-droplet morphology with weak interfacial adhesion between the phases, resulting in complete thermodynamical incompatibility of this polymer blend [31].



(a) (b) (c)

Figure 2. SEM images of film samples based on PLA/EVA blends with: (a) 20PLA/80EVA; (b) 50PLA/50EVA; and (c) 80PLA/20EVA wt.% of PLA at a magnification of 20000×.

Raman microscopy was used to study the chemical nature of continuous and discontinuous phases of polymers with varying compositions of PLA/EVA blends. The study was carried out on the cleavage of film samples of blends to assess the bulk structure of the materials. Multidimensional analysis made it possible to obtain Raman spectra at separate points, showing the distribution of each component simultaneously [32,33].

Figure 3 shows the obtained Raman spectra for the blend samples with 20, 50, and 80 wt.% of PLA. The strong Raman bands in the 3100–2800 cm^{-1} range correspond to C–H stretching modes of the $–CH_3$ group of PLA. The CH_3 stretching modes appeared at 3014 and 2960 cm^{-1}. The C–H stretching mode was observed at 2877 cm^{-1}, which is consistent with previous literature [34]. Raman spectra of EVA reveal a series of bands originating from stretching C–H vibrations of $–CH_3$ (2930 cm^{-1}) and $–CH_2$ (2848 and 2885 cm^{-1}) [35].

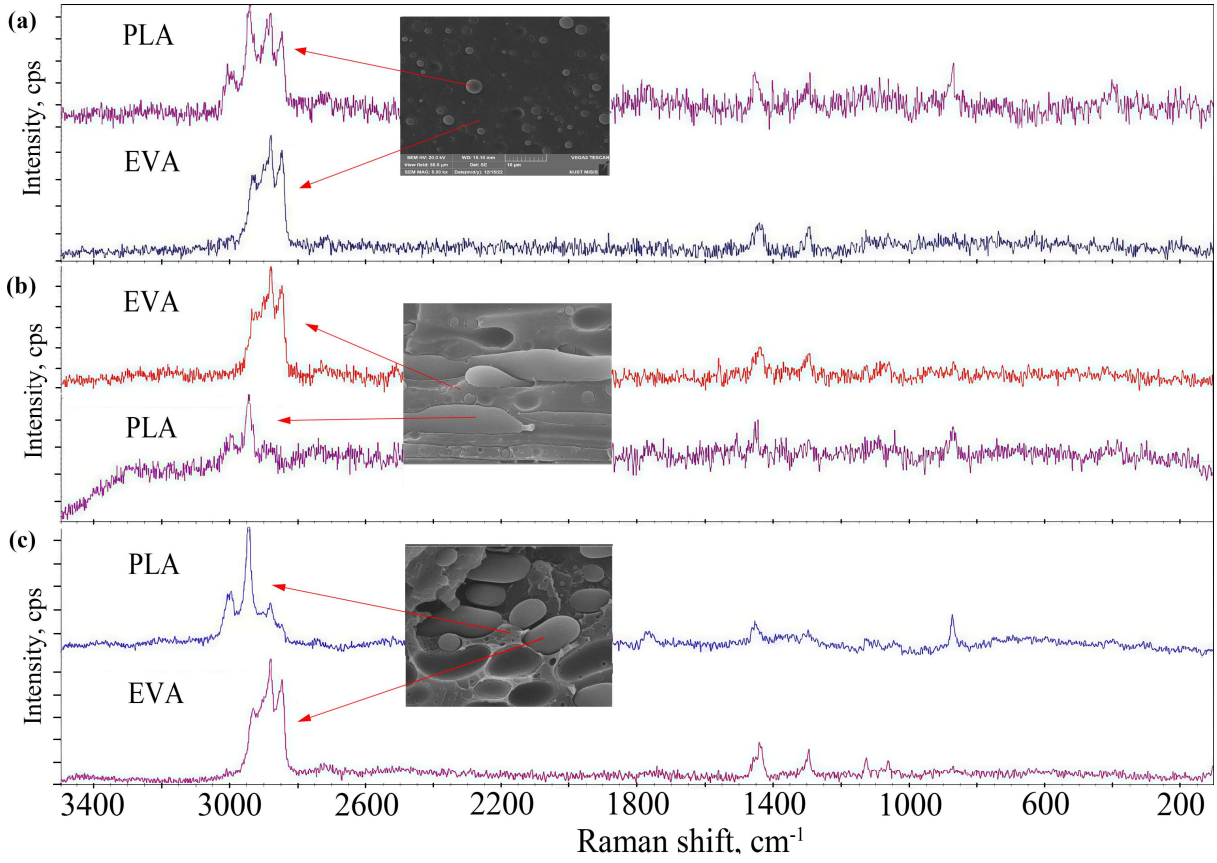


Figure 3. Raman microscopy for the blends of: (a) 20PLA/80EVA; (b) 50PLA/50EVA; and (c) 80PLA/20EVA (wt.%) (cross-sections).

According to the analysis results, it was defined that for the samples with a higher content of PLA, this polymer was a matrix (continuous phase) with EVA domains included. On the contrary, the samples with lower PLA content were an EVA matrix with PLA domains included, which is a predictable result. The blend with an equal content of both components (50PLA/50EVA) was predominantly characterized by co-continuous morphology. However, areas with a discrete phase of PLA were observed, which is probably due to the discrepancy between the weight and volume content of the used polymers. The phase reversal range in PLA/EVA blends was more than 30 wt.% and less than 60 wt.% of PLA. Similar phase inversion ranges have previously been found for other polymer pairs [36,37].

In order to analyze the compatibility and interaction of PLA and EVA in the blends, an FTIR (ATR method) was performed. The obtained IR-spectra of the blends are shown in Figure 4. The absorption band corresponding to the vibrations of the carbonyl groups (C=O stretching vibrations) has different

maxima for both polymers [38]. So, for PLA, the maximum absorption band is at 1755 cm^{-1}, and for EVA it is at 1735 cm^{-1}. Figure 4 shows that for the blends with 20–50 wt.% PLA, the absorption peak in the region of 1720–1760 cm^{-1} moved to the region of large wavenumbers relative to the peaks of neat PLA and EVA. At the same time, a wide peak appeared in the region of 3000–3600 cm^{-1}, associated with stretching vibrations of hydroxyl (O–H) groups. The variations within this region are sensitive to hydrogen bonding and bound water within the structure. Apparently, it appears to be characteristic of blends with less than 50 wt.% PLA due to altered diffusion properties caused by the increased accessibility into the interfacial layer, which can be seen by density measurements. In the case of more than 50 wt.% PLA, this process is blocked by the glassy matrix of PLA.

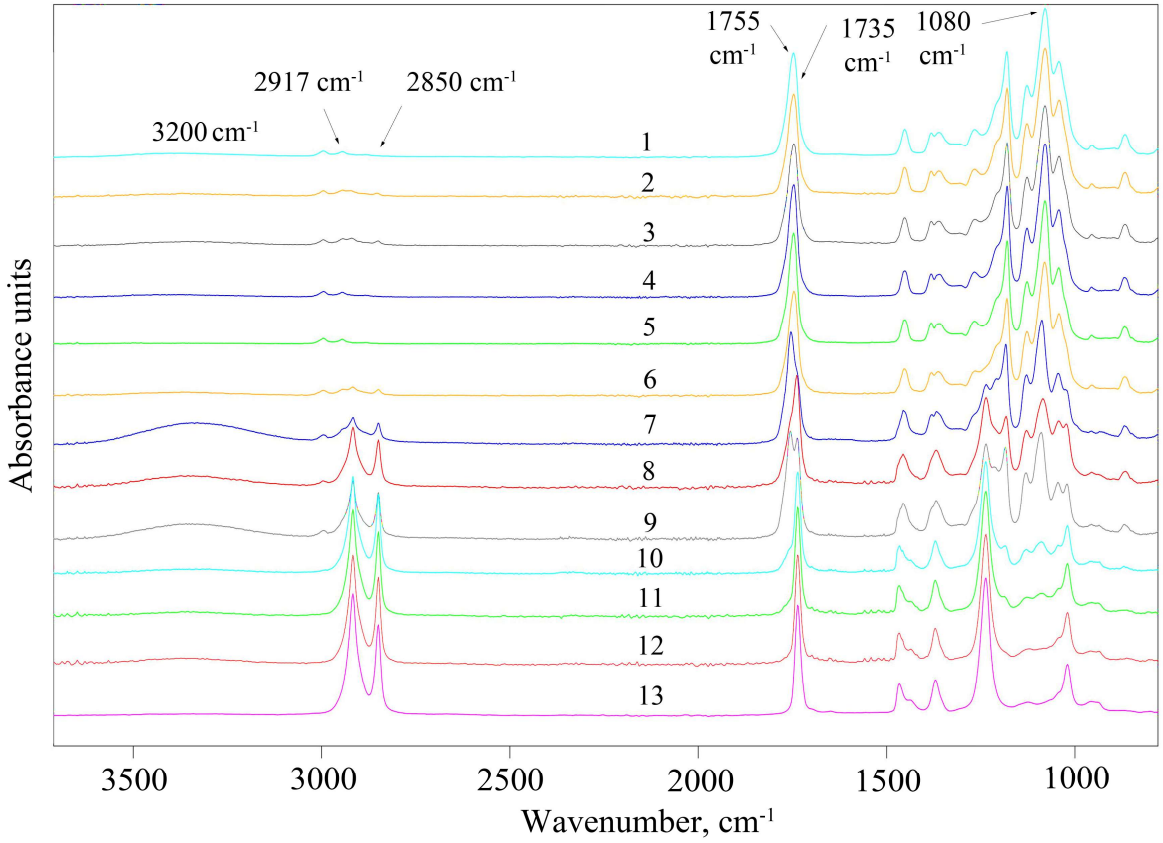


Figure 4. FTIR spectra (ATR mode) for the film samples based on: (curve 1) neat PLA; (curve 13) neat EVA; and their blends: (curve 2) 95PLA/5EVA; (curve 3) 90PLA/10EVA; (curve 4) 80PLA/20EVA; (curve 5) 70PLA/30EVA; (curve 6) 60PLA/40EVA; (curve 7) 50PLA/50EVA; (curve 8) 40PLA/60EVA; (curve 9) 30PLA/70EVA; (curve 10) 20PLA/80EVA; (curve 11) 10PLA/90EVA; and (curve 12) 5PLA/95EVA (wt.%) (surface of the films).

Due to the fact that the absorption bands at 1755 and 1735 cm^{-1} overlap, for quantitative calculations, two additional absorption bands were selected, which differ for PLA (1080 cm^{-1}) and EVA (2917 cm^{-1}). The peak at 1080 cm^{-1} is a key characteristic band for PLA and attributed to C–O stretching vibrations within the polymer chain [39]. The 2917 cm^{-1} peak in an FTIR-spectrum of

EVA is typical of polyolefins and corresponds to the asymmetric stretching vibration of the C–H bonds in methylene groups (–CH_2) [40].

To analyze the polymer distribution in the film's near-surface layers, the ratios of the intensity of the absorption bands I_{1755}/I_{1735} and I_{1080}/I_{2917} were determined. The results are presented in Figure 5. It was shown that for blends with a PLA content of more than 40 wt.%, PLA predominates on the surface of the films.

The observed fact can be explained by the lower viscosity of the PLA melt compared to the EVA melt. As a result, when cooling, the PLA tends to migrate to the surface of the material (segregate), concentrating in the near-surface layers and reducing system energy. Similar patterns have been previously shown [41,42]. Furthermore, when pressing samples from PLA/EVA blends on a highly polar cellophane substrate, the more polar PLA component can be preferentially attracted to the substrate, forming a surface adsorption layer that is then *frozen in* by quenching. This phenomenon can occur across the entire concentration. A local decrease in the concentration of PLA in the volume of the material can lead to the formation of a discrete polymer phase, even for blends with an equal content of both components (PLA and EVA), which was observed in the results of Raman microscopy.

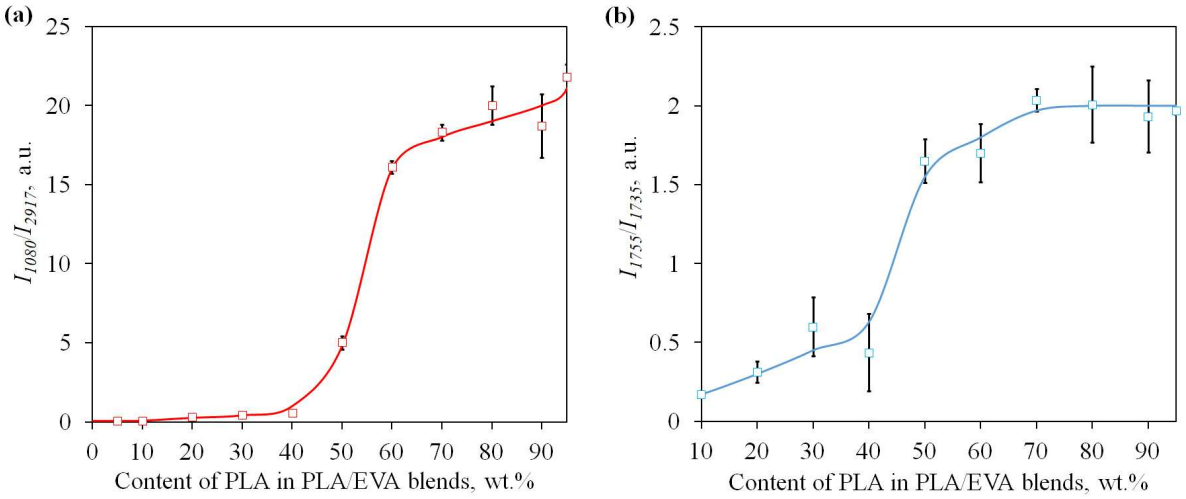


Figure 5. Ratios of the intensity of absorption bands: (a) I_{1080}/I_{2917} and (b) I_{1755}/I_{1735}. The bands at 1755 and 1080 cm^{-1} are characteristic for PLA, and those at 1735 and 2917 cm^{-1} are characteristic for EVA.

Thermal properties and phase structure of the PLA/EVA blends were analyzed using the DSC method. Figure 6 shows DSC curves of the neat PLA and their blends with EVA obtained at the first heating of the samples. The character of the DSC curves at the second heating does not differ from that of the first heating. The total melting and crystallization parameters of PLA are presented in Table 4.

During the heating of the PLA/EVA blends, several transitions are observed in the range from 50 to 160 °C, related to the following processes: EVA melting (50–80 °C); PLA glass transition (55–60 °C); PLA cold crystallization (90–115 °C); and PLA melting (135–155 °C).

In this study, EVA with a higher percentage of vinyl acetate (28 wt.%) resulted in very low crystallinity (VA units disrupt the crystalline structure of the polyethylene) [43]. For this EVA, a

gently sloping peak at approximately 50–80 °C was observed. The endset temperature of EVA melting was approximately 80 °C. In a similar temperature range, the PLA glass transition occurred. This was followed by the recrystallization of PLA (the so-called cold crystallization). In the case of PLA/EVA blends, this process took place in the presence of molten liquid EVA, which could act as a plasticizer for PLA, contributing to the improvement of crystallites. As a result, the structure of PLA crystallites changed under the influence of EVA addition.

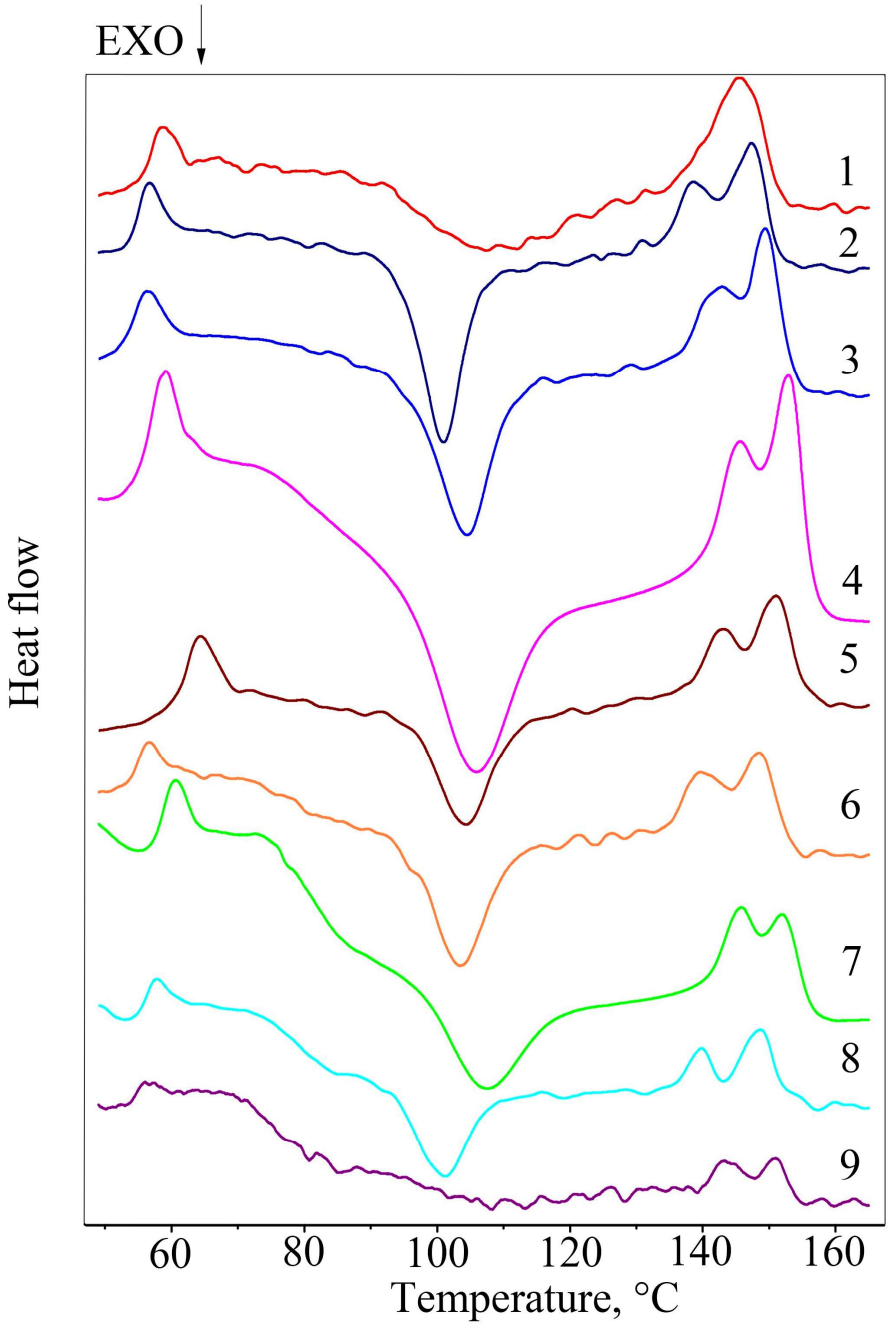


Figure 6. DSC curves (first heating) of: (curve 1) neat PLA and PLA/EVA blends: (curve 2) 95PLA/5EVA; (curve 3) 90PLA/10EVA; (curve 4) 80PLA/20EVA; (curve 5) 70PLA/30EVA; (curve 6) 60PLA/40EVA; (curve 7) 50PLA/50EVA; (curve 8) 40PLA/60EVA; and (curve 9) 30PLA/70EVA (wt.%).

Table 4. Thermal parameters of PLA as a neat polymer and of its blends with EVA (first heating, cooling, and second heating). DSC data normalized to the mass of PLA.

PLA content in PLA/EVA blend, wt.%	Glass transition		Crystallization						Melting			
	T, °C (Δ ± 0.2 °C)		*T*, °C (Δ ± 1 °C)			*ΔH*, J g^{-1} (Δ ± 3 J g^{-1})			*T*, °C (Δ ± 1 °C)		*ΔH*, J g^{-1} (Δ ± 3 J g^{-1})	
	1st heat	2^{d} heat	1st heat	Cool	2^{d} heat	1st heat	Cool	2^{d} heat	1st heat	2^{d} heat	1st heat	2^{d} heat
100	57.2	56.5	108	58	116	–24	–	32	146*	146*	23	32
95	54.7	50.1	101	52	101	–41	–	38	139/147	136/145	34	38
90	54.7	54.4	105	52	110	–35	–	38	143/149	141/149	32	38
80	55.7	52.6	111	53	115	–29	–29	34	144/149	145/150	32	34
70	60.3	54.2	108	52	117	–34	–23	28	143/149	147/152	31	28
60	54.9	54.4	103	51	113	–41	–27	37	140/149	140/149	35	37
50	57.1	58.1	112	52	115	–24	–25	36	145/150	144/150	37	36
40	56.5	54.5	101	50	110	–37	–26	32	140/149	141/149	37	32
30	54.8	–	–	51	–	–20	–23	–	144/151	–	25	–
20	–	–	–	50	–	–	–23	–	–	–	–	–

Note: *T:* temperature; *ΔH*: enthalpy; 1st heat: first heating run; 2^{d} heat: second heating run; cool: first cooling run; *: the melting peak is monomodal.

Crystalline polymorphism is typical for PLA (L-isomer). PLA can form different crystalline structures, the most common being the *α*-form [44,45]. In this study, the thermogram of the neat PLA demonstrated a single endothermic peak. Adding EVA to PLA resulted in a bimodal-melting behavior of PLA. As can be seen, even the DSC curve of the 95PLA/5EVA blend demonstrated another melting behavior compared to the neat PLA. Thus, the role of EVA in the observed pattern is obvious.

It is known that the bimodal melting peak of PLA often results from a melt-recrystallization process, where the low-temperature peak is due to the melting of original crystallites, and the high-temperature peak is due to new crystallites formed during heating (cold crystallisation process) [46,47].

The DSC curves of the blends show that both melting changes and cold crystallization character changed. M. Yasuniwa et al. showed that as the cold crystallization temperature shifted to a lower temperature range, the crystallization rate increased [48]. The addition of EVA lowered the melting point of PLA, which was due to the formation of crystallites of a different, less perfect form. The cold crystallization enthalpy also increased by 2–3 times for blends with 60, 90, and 95 wt.% PLA, which exhibited the lowest cold crystallization temperatures.

It is important to note that the initial material samples were obtained by rapid cooling from the melt and are completely amorphous (as confirmed by WAXD). The double melting peaks observed in the first heating run of DSC (Figure 6) are due to cold crystallization occurring during the DSC scan itself. Clearly, the addition of EVA to PLA alters the nature of the cold crystallization, acting as a plasticizer. The reorganization of the PLA structure in the presence of EVA during heating in the DSC analysis leads to the appearance of a bimodal melting peak for PLA [49].

It was assumed that the bimodal melting peak of PLA could arise from the melting of two different forms of crystallites, with the low-temperature peak associated with the melting and phase

transition of the δ (or α') form, and the high-temperature peak associated with the more stable α form. Further, the presence of two crystalline polymorphs associated with the α and α' phases was proven by the X-ray diffraction method.

Figure 7 shows X-ray diffraction patterns of the neat PLA (curve 1), EVA (curve 2), and 50PLA/50EVA (curve 3) recorded in the Bragg-Brentano geometry. In transmission geometry, practically identical diffraction patterns of these films without any diffraction lines characteristic of crystalline structures were recorded. Therefore, according to X-ray diffraction, all these films could be considered as amorphous. The diffraction pattern of the 50PLA/50EVA blend can be obtained by summing the diffraction patterns of the neat PLA and the neat EVA. Consequently, in this blend, the polymers form their own distinct amorphous phases.

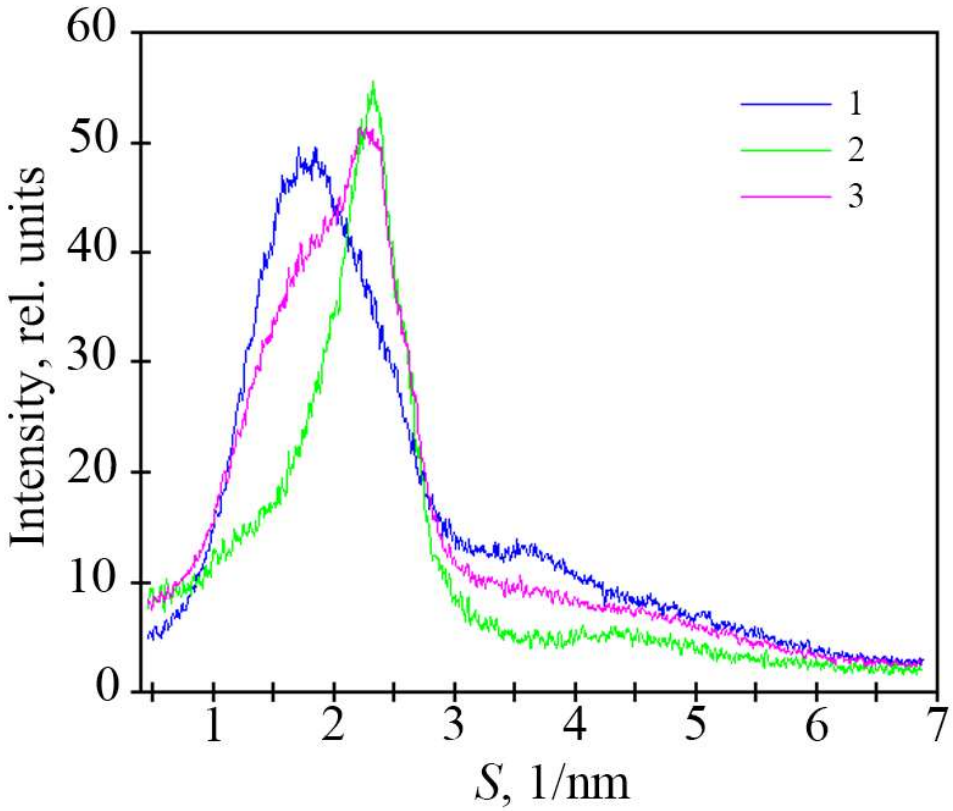


Figure 7. X-ray diffraction patterns of: (curve 1) neat PLA; (curve 2) neat EVA; and (curve 3) 50PLA/50EVA blend films. Intensity is plotted versus the diffraction vector modulus (S) = ($2\sin\theta$)/λ, where θ is half the diffraction angle, and λ is the X-ray wavelength.

The effect of annealing on the neat PLA and the PLA/EVA blend structure was studied mainly by X-ray diffraction in the transmission geometry on the diffractometer with a position-sensitive detector, which increases the measurement speed and allows to study small samples with uneven surfaces. The resulting diffraction patterns are shown in Figures 8 and 9. The films containing 90 wt.% PLA (PLA90/EVA10) were also studied after annealing at 80 and 130 °C using the Bragg-Brentano geometry, which provides a higher angular resolution. Diffraction patterns obtained using the Bragg-Brentano and transmission methods were almost identical.

For the neat PLA and the PLA/EVA blend, a partial crystallization of PLA occurred as a result of annealing for 1.5 h at 80 or 130 °C. The diffraction patterns of PLA (Figure 8a, curve 1) and PLA/EVA blends containing 5, 10, and 20 wt.% EVA (Figure 8b–d) obtained after annealing at 80 °C contained similar diffraction peaks, indicating an appearance of a PLA crystalline structure in these samples. The two main diffraction peaks were located at $S \approx 1.86$ nm^{-1} and $S = 2.13$ nm^{-1} (for Cu-Kα radiation, these S values correspond to $2\theta \approx 16.5$ and $2\theta \approx 18.9^{o}$). The diffraction peaks of very low intensity may be distinguished at $S \approx 1.67$, 2.5, 2.8, 3.1, 3.26, and 3.5 nm^{-1} ($2\theta \approx 14.8$, 22.2, 24.9, 27.7, 29.1, and 31.3°). The differences in the intensity of diffraction peaks observed in Figure 8 for different samples can be explained by the difference in PLA content in these films.

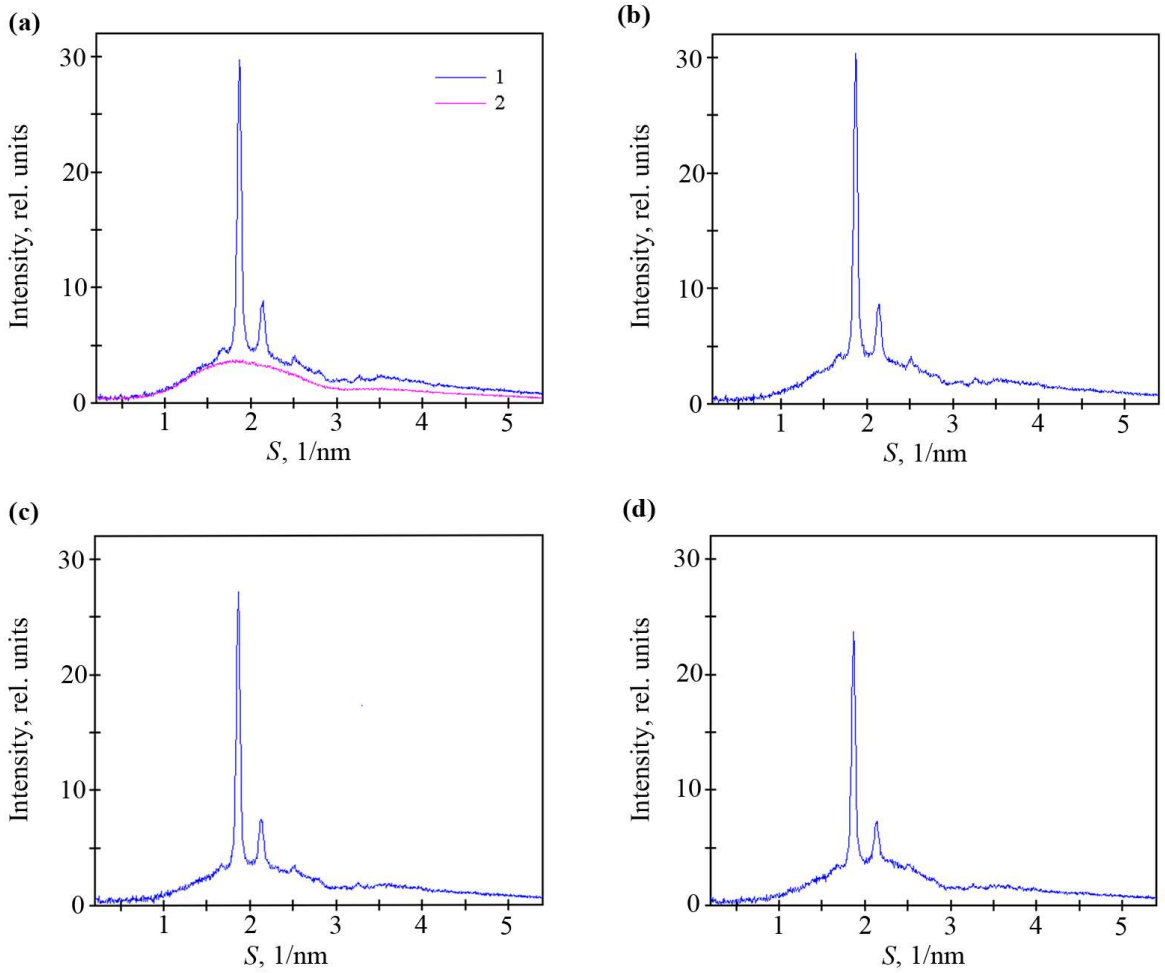


Figure 8. X-ray diffraction patterns of: (a, curve 1) neat PLA; (b) 95PLA/5EVA; (c) 90PLA/10EVA; and (d) 80PLA/20EVA blends after annealing for 1.5 h at 80 °C. The diffraction pattern of neat PLA film was scaled to represent the intensity of the amorphous part of the (a, curve 2) annealed PLA film and used for calculation of PLA crystallinity in the annealed film.

The diffraction patterns of PLA/EVA blend films annealed at 130 and 80 °C were generally similar. However, after annealing at 130 °C, a slight shift of diffraction peaks toward larger S values (approximately for 0.015–0.02 nm^{-1}) occurred, the intensity of low-intensity peaks at $S \approx 1.67$, 2.5, 2.8, 3.1, 3.26, and 3.5 nm^{-1} increased, and the appearance of some additional

low-intensity peaks (for instance, at $S \approx 1.4$ and 2.7 nm^{-1}) was observed. The diffraction patterns of 90PLA/10EVA and 95PLA/5EVA blend films annealed at 130 °C are shown in comparison with the diffraction patterns of these films annealed at 80 °C in Figure 9. Evidently, crystalline structures of PLA/EVA blends annealed at 80 and 130 °C were similar but not identical. Analogous changes of the X-ray diffraction pattern of the neat PLA with an increase in annealing temperature were observed in other studies [50].

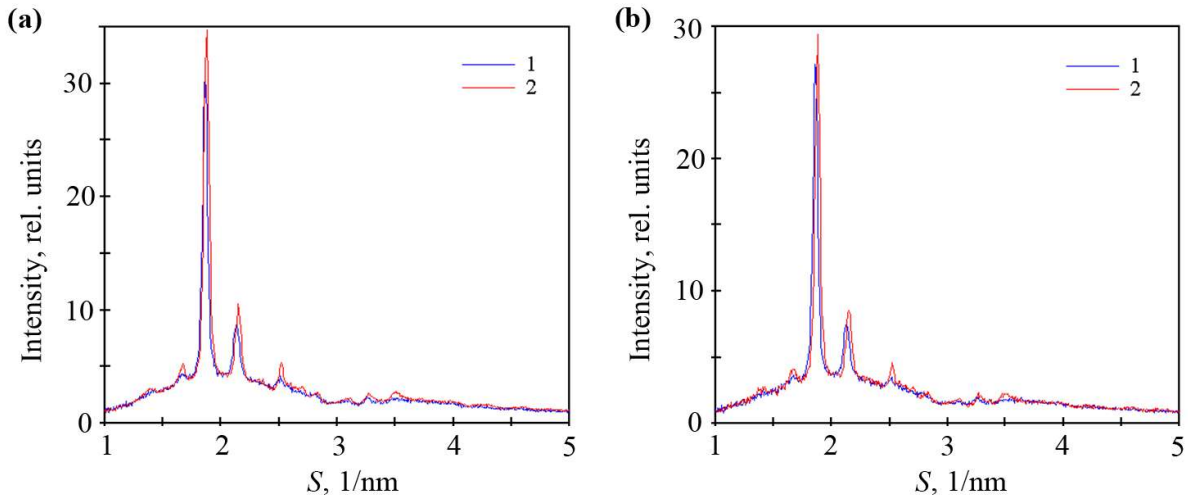


Figure 9. X-ray diffraction patterns of: (a) 95PLA/5EVA; and (b) 90PLA/10EVA blend films after annealing for 1.5 h (curve 1) at 80 °C and (curve 2) 130 °C.

Such a difference in X-ray diffraction patterns, as observed for PLA/EVA blend films after annealing at 80 and 130 °C (Figure 9), apparently corresponds to different crystallite forms of PLA, namely to a rather disordered α'-form after annealing at 80 °C and to a higher ordered α-form after annealing at 130 °C [51]. These crystallite forms are considered to be most probably orthorhombic with very similar unit cell parameters a, b, c, equal to 1.0683, 0.6170, 2.8860 nm for the α-form and to 1.080, 0.620, 2.880 nm for the α'-form, respectively [52–54]. The diffraction peaks with positions that may correspond to experimental positions of the two main diffraction peaks of PLA/EVA blend films were calculated using these parameters of the PLA crystal unit cells of α- and α'-forms (Table 5). It follows from Table 5 that experimental positions of the diffraction peaks for PLA/EVA blend films after annealing at 80 °C correspond to the PLA crystal α'-form, and after annealing at 130 °C to the α-form. However, the possibility of coexistence of α- and α'-forms cannot be completely excluded, with predominance of the α'-form after annealing at 80 °C and predominance of the α-form after annealing at 130 °C.

Table 5. Experimental positions of the main diffraction peaks (S_{exp}) on the diffraction patterns of PLA/EVA blend films, obtained after annealing at 80 and 130 °C, and positions (S_{calc}) of corresponding diffraction peaks calculated for crystal α- and α'-forms of PLA using the unit cell parameters determined for these forms in the work [52,53].

	S_{exp}, nm^{-1}		Miller indices (*hkl*)	S_{calc}, nm^{-1}	
	80 °C	130 °C		α-form	α'-form
Peak 1	1.861	1.877	110	1.8716	1.8598
			200	1.8721	1.8519
Peak 2	2.131	2.149	014	2.1326	2.1285
			113	2.1409	2.1316
			203	2.1414	2.1247

For a more detailed comparison of some structural characteristics of annealed PLA/EVA blend samples with different EVA contents, the experimental profiles of the main diffraction peaks ($S \approx 1.86$ and 2.13 nm^{-1}) were approximated by Gaussian functions. Then, peak positions (S_{max}), peak integral widths (ΔS), and peak integral intensities (I_{int}) were determined. After, I_{int} was divided by the mass fraction of PLA in the films; this way, the integral intensities of these peaks normalized to one and the same mass of PLA ($I_{int/norm}$) were obtained.

The average PLA crystallite size (L_{hkl}) in the samples was assessed as $L_{hkl} = [(\Delta S)^2 - (\Delta S_{instr})^2]^{-1/2}$, where ΔS is the integral width of PLA *hkl* diffraction peak, and ΔS_{instr} is the integral width of corundum 012 diffraction peak, determined by fitting of this peak with a Gaussian function and used as instrumental broadening of PLA diffraction peaks. Resulting values of S_{max} and L_{hkl} are given in Table 6.

The values $I_{int/norm}$ were determined as outlined above, related to the same mass of PLA in the samples. Therefore, the ratios of $I_{int/norm}$ for different samples with the same crystal structure give the relative values of PLA crystallinity in these samples. The degree of crystallinity (C) of the neat PLA sample annealed at 80 °C was calculated using the relation $C = (I_{exp} - I_{am})/I_{exp} \times 100\%$, where I_{exp} is the integrated experimental intensity of the sample, and I_{am} is the integrated intensity of the amorphous part of the sample. The intensities of crystalline and amorphous parts of PLA were separated for such calculation using the diffraction pattern of the neat amorphous PLA scaled to represent the intensity of the amorphous part of the annealed PLA film, as shown in Figure 8a (curve 2). The degree of crystallinity for the neat PLA film annealed at 80 °C calculated in such a way was $C = 37\%$. Using this C value and the ratios of $I_{int/norm}$ for this and another samples, PLA degree of crystallinity in all the samples was calculated (Table 6).

The obtained results (Table 6) confirm that PLA crystalline structure in the neat PLA and all studied PLA/EVA blends (PLA content of 95, 90, and 80 wt.%) after annealing at 80 °C is the same. For all these samples, the positions of the main diffraction peaks coincide with an accuracy higher than ±0.1% (1.859–1.862 nm^{-1} for the first peak, and 2.129–2.132 nm^{-1} for the second peak). Therefore, the PLA crystal lattice parameters in all these samples may be considered to be identical. The exact coincidence of diffraction peaks for these samples also implies that if any coexistence of α- and α'-forms takes place in these samples, the proportion of α- and α'-forms in these samples is the same. An average PLA crystallite size for all the films annealed at 80 °C was also approximately the

same: $L_{110/200}$ = 25–27 nm and $L_{014/113/203}$ = 17–19 nm (Table 6). Possibly, PLA crystallite size increased slightly (for ~2 nm) under EVA addition (Table 6).

The effect of the annealing at 130 °C onto the structure of PLA/EVA blends was studied for the 95PLA/5EVA and 90PLA/10EVA samples. After annealing, the positions of the main diffraction peaks changed as compared with the samples annealed at 80 °C: from 1.859–1.862 to 1.877 nm^{-1} and from 2.129–2.132 to 2.148–2.149 nm^{-1}, respectively (Table 6). This confirms the transformation of PLA crystal structure from the α'-form to the α-form under the increase in annealing temperature from 80 to 130 °C (Table 5). PLA crystallite size $L_{110/200}$ after annealing at 130 °C had not noticeably changed as compared with annealing at 80 °C (Table 6), and PLA crystallite size $L_{014/113/203}$ slightly increased (from 17–19 to 22–23 nm).

The PLA degree of crystallinity for all the samples did not differ significantly. C values determined for PLA/EVA blends annealed at 80 °C on the basis of 110/200 peak intensity analysis were equal to ~38% ± 2% (Table 6), and this C variance lies within the error of its determination. Both 95PLA/5EVA and 90PLA/10EVA blends annealed at 130 °C had a PLA crystallinity of ~43%, and this value was somewhat higher (~5%) than for the sample annealed at 80 °C (Table 6). Similar values of PLA crystallinity in PLA/EVA blends were also obtained by the 014/113/203 peak intensity analysis (Table 6). The similarity of the diffraction patterns recorded in the Bragg-Brentano and transmission geometries also confirmed that PLA crystallites in the studied films had no preferred orientation.

According to the X-ray diffraction data, PLA and EVA in the blends exist as two separate amorphous phases. The type of crystallite lattice, average crystallite size, and degree crystallinity of PLA in the presence of EVA remain the same for the native and annealed samples. A cold crystallization of PLA in the PLA/EVA blends with 5, 10, and 20 wt.% EVA led to the formation of the crystalline α'-form at 80 °C or the crystalline α-form at 130 °C. The average crystallite size and degree of crystallinity for PLA of these crystal forms are rather similar. The coexistence of these two PLA crystallite forms in PLA/EVA blends appearing at cold crystallization may explain a double PLA melting peak observed in the DSC thermograms.

Table 6. Positions (S_{max}) of two main X-ray diffraction peaks, average crystallite size and degree of crystallinity determined for PLA as a neat polymer and in PLA/EVA blends annealed for 1.5 h at 80 or 130 °C (the values of L_{hkl} and C were evaluated by the analysis of these peaks' integral width and intensity).

Sample composition and annealing temperature	Diffraction peak 110/200			Diffraction peak 014/113/203		
	S_{max}, nm^{-1}	L_{hkl}, nm	C, %	S_{max}, nm^{-1}	L_{hkl}, nm	C, %
PLA, 80 °C	1.862	25.1	37.0	2.132	17.4	37.0
95PLA/5EVA, 80 °C	1.862	27.1	39.6	2.132	18.5	39.4
90PLA/10EVA, 80 °C	1.859	27.2	37.3	2.129	19.0	36.2
80PLA/20EVA, 80 °C	1.861	27.4	36.0	2.131	18.6	36.4
95PLA/5EVA, 130 °C	1.877	25.1	42.8	2.148	22.3	41.1
90PLA/10EVA, 130 °C	1.877	26.0	42.9	2.149	22.7	42.5

The results of mechanical and MFI tests are presented in Figure 10 and Table 7. Also, representative curves of the stress strain tests are presented in Figure 11. The addition of PLA to neat EVA did not significantly affect the mechanical properties of EVA. The relative elasticity decreased by 20% for the 30PLA/70EVA blend (500%) compared to the neat EVA (620%). Further, with more 30 wt.% PLA in the blend, there was a significant change in strength and elongation at break, associated with phase inversion (a transition from one continuous phase to another). For the blends with PLA content higher than 30 wt.% and less than 60 wt.%, negative deviations from additivity were observed for the dependences of tensile strength and elongation on the blend composition. For PLA-rich blends, even adding 5 wt.% EVA to PLA significantly worsened the mechanical properties of the films. At low EVA content in the PLA matrix, the EVA forms small-sized particles (domains) within the PLA, resulting in a large interfacial area. However, because the adhesion between the phases is weak (as evidenced by SEM images), phase separation occurs, leading to the formation of defective zones at the interface; these zones serve as the sites where fracture initiates during deformation [55].

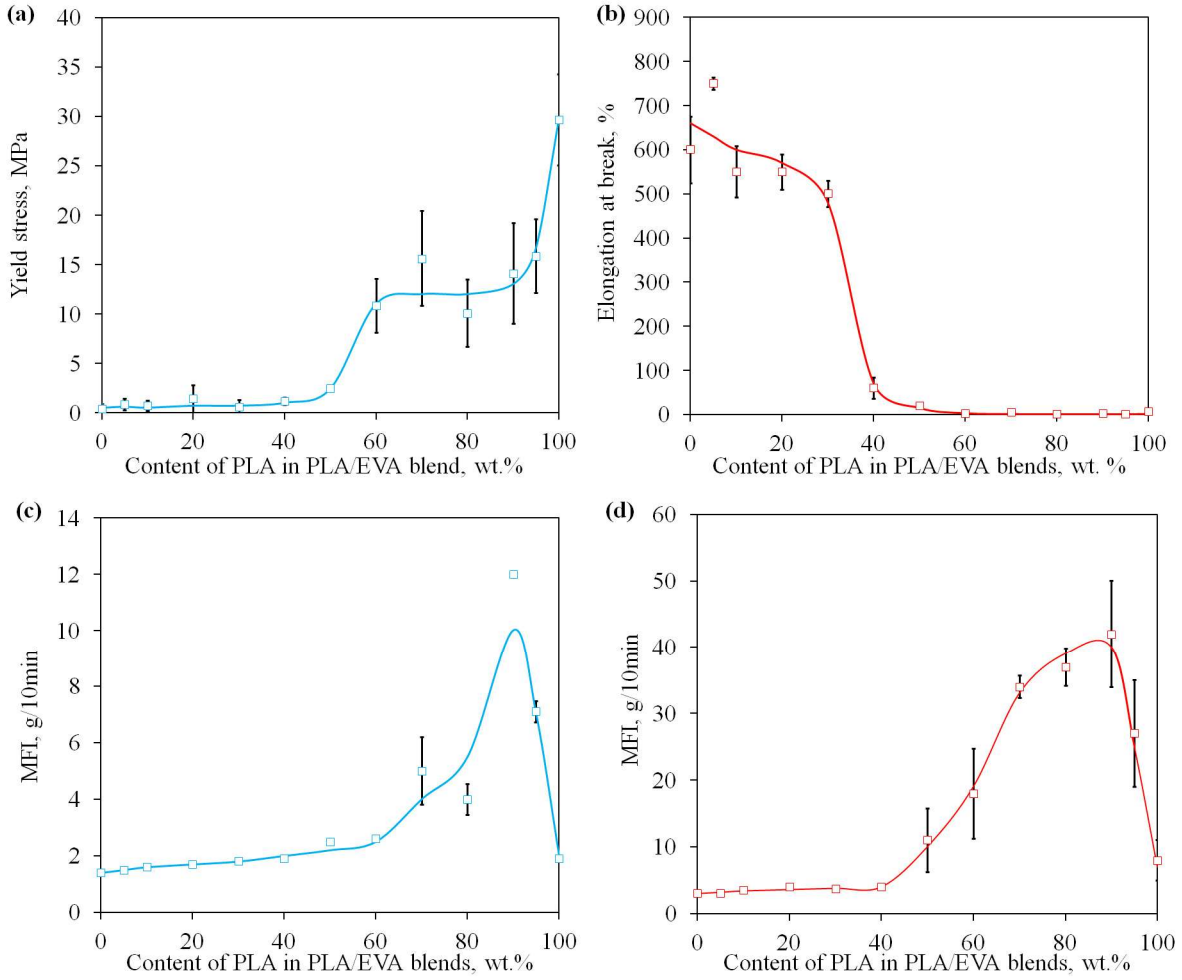


Figure 10. Dependences of: (a) yield stress; and (b) relative elongation at break on the PLA/EVA blend composition (tensile tests) and MFI at 170 °C, with a load of: (c) 1.23 kg or (d) 2.16 kg on the PLA/EVA blend composition.

Table 7. Mechanical properties of the PLA/EVA blends (under tension).

Content of PLA in PLA/EVA blend, wt.%	Yield stress, MPa		Tensile strength at break, MPa		Elongation at break, %		Young`s modulus, MPa	
	Average	SD	Average	SD	Average	SD	Average	SD
100	29.7	4.6	34.1	1.0	6.4	3.6	4920	340
95	15.9	3.7	25.4	5.5	0.9	0.1	2990	640
90	14.1	5.1	21.8	5.5	2.7	3.3	2150	380
80	10.1	3.4	20.5	4.1	1.3	0.4	2115	200
70	15.6	4.8	21.3	3.0	4.3	2.3	1920	320
60	10.8	2.7	12.5	2.6	2.7	0.7	1380	210
50	2.5	0.1	3.6	0.5	20.0	6.9	244	54
40	1.2	0.6	2.8	0.5	60.0	21.7	125	72
30	0.6	0.2	4.7	2.1	500.0	23.8	19	3.4
20	1.4	0.4	4.5	1.0	550.0	40.0	15	5.0
10	0.7	0.2	7.0	1.4	550.0	57.6	9	3.3
5	0.9	0.2	5.2	0.4	790.0	13.7	11	1.5
0	0.3	0.1	7.1	3.4	620.0	74.9	12	2.5

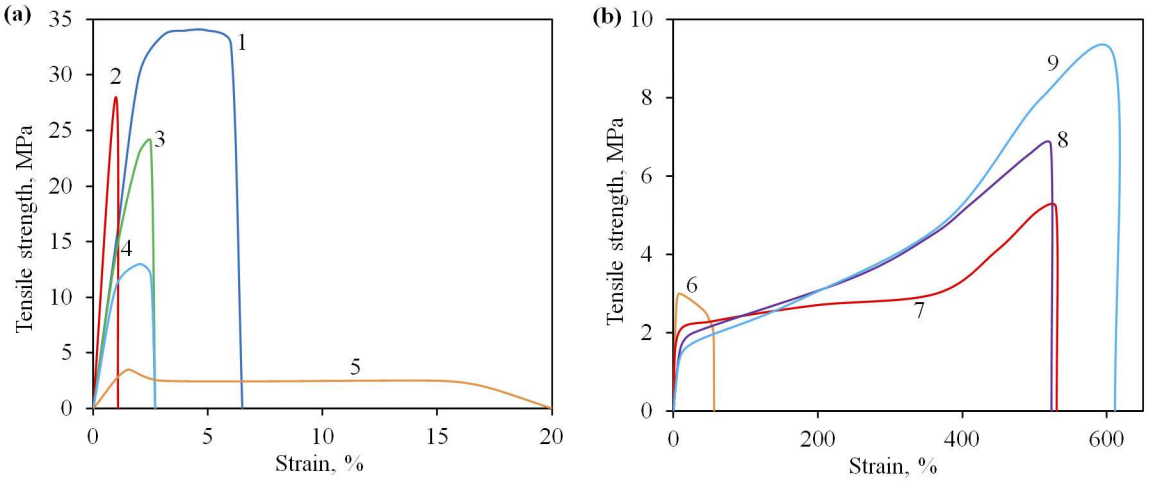


Figure 11. Stress–strain tests of the PLA/EVA blend composition: (curve 1) neat PLA; (curve 2) PLA90/EVA10; (curve 3) PLA80/EVA20; (curve 4) PLA60/EVA40; (curve 5) PLA50/EVA40; (curve 6) PLA40/EVA60; (curve 7) PLA30/EVA70; (curve 8) PLA10/EVA90; and (curve 9) neat EVA (wt.%).

A similar dependence of the mechanical properties on the composition of the polymer blends has been shown in other papers. For instance, it has been observed that the addition of EVA at >10 wt.% does not cause changes [56] until phases inversion.

The MFI value of the blends were determined at a polymer compounding temperature (170 ± 1 °C) to define component interactions during the blend production. Two different loads of 1.23 and 2.16 kg were used for testing. Both obtained MFI dependences on the blend composition were similarly non-additive—a roughly parabolic relationship with composition (Figure 10c,d). A positive deviation

from additivity was found for the blends with PLA content from 50 to 95 wt.%, which indicates a decrease in melt viscosity compared to neat polymers.

The discovered dependence can be explained by the phenomenon of interfacial slip. When two immiscible polymers are mixed (for example, PLA and EVA), the interface has fewer entanglements, creating a low-viscosity layer. When shearing, this layer allows for slippage, significantly reducing the overall viscosity of the blends [57].

As can be seen from Figure 10, the increase in MFI was clear for the blends with a predominant content of PLA, where EVA acts as an effective plasticizer. This peak in fluidity was most likely associated with a higher dispersion of the EVA phase, i.e., a larger interphase surface area. Although the addition of a more viscous polymer (EVA) should increase the viscosity of PLA/EVA blends, the elasticity ratio of polymer components is a more critical factor in the phase inversion and morphology development of immiscible polymer blends, surpassing the predictive capability of viscosity alone [58]. The plasticizing effect of these well-dispersed EVA domains significantly lowers the melt viscosity, leading to the highest MFI value at the 90/10 ratio [59].

According to the results of density determination (Figure 12) by hydrostatic weighing, a negative deviation from additivity was observed on the curve of dependence of density on the composition of the blends with 20–60 wt.% PLA (Figure 12). PLA and EVA have limited compatibility, so their blending can create structural irregularities that hinder close packing, similar to how branches reduce crystallinity in single polymers, thus lowering density. Moreover, according to the density indicator, polymer compatibility is higher in the blends with a higher PLA content. It correlates with another study [56] that stated that an EVA content exceeding 20 wt.% decreases the mechanical properties of blends and leads to a different blend morphology due to immiscibility.

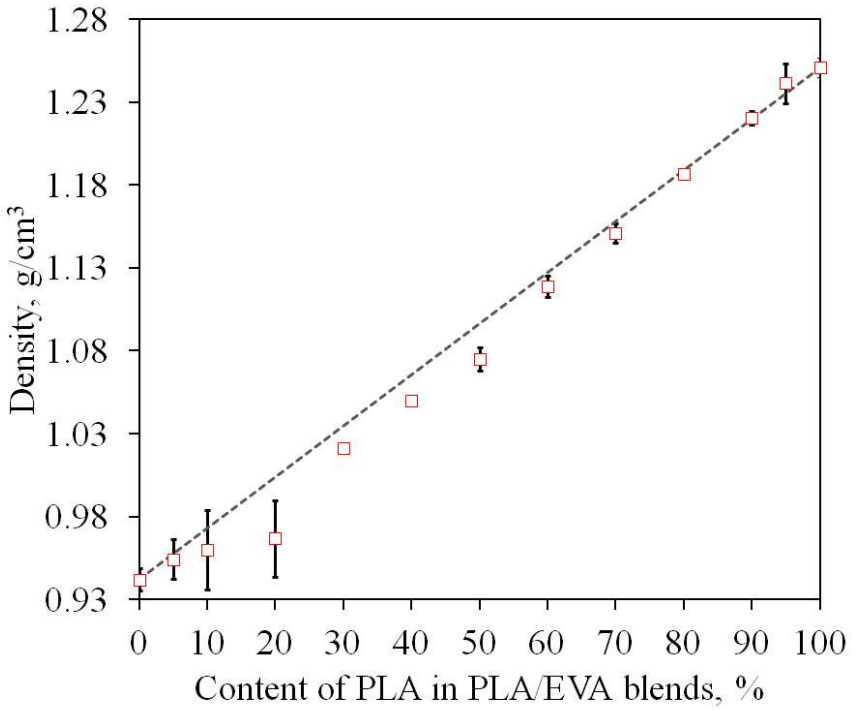


Figure 12. Dependence of density on the PLA/EVA blend composition.

4. Conclusions

In this work, polymer blends based on polylactide and ethylene-vinyl acetate copolymer containing 28 wt.% of vinyl acetate have been investigated. The effect of blend composition on the phase structure and properties has been established.

Each component forms a continuous matrix when its content in the blend is over 60 wt.%, while the second component (up to 40 wt.%) exists as a dispersed phase. Furthermore, the PLA domains within the EVA matrix are 2–3 times smaller than the EVA domains within the PLA matrix (2–4 and 6–7 μm, respectively). In the composition range of 30–60 wt.% of PLA, a co-continuous phase morphology was found by SEM photos for 40PLA/60EVA and 50PLA/50EVA, where each component forms a co-continuous morphology. An elevated concentration of PLA, exceeding its bulk content in the blend, is on the surface of the samples.

The EVA component exerts a plasticizing effect on the glassy PLA matrix. With an EVA content of only 5 wt.%, the cold crystallization of PLA is accelerated. As a result of cold crystallization, two crystalline modifications of PLA (α and α') are formed. This has been confirmed by WAXD data. The presence of two crystalline forms does not affect the formation of the blend phase structure.

Mechanical testing has revealed that the addition of PLA to EVA slightly decreases the elongation at break (by 20% for the 30PLA/70EVA blend compared to ε = 620% for the neat EVA). When the EVA content exceeds 30 wt.%, phase inversion occurs, causing a ten-fold reduction in elongation at break. On the contrary, the addition of even 5 wt.% of EVA to PLA sharply reduces the strength parameters of the material, which is likely driven by the difference in the dispersed phase particle size. An increase in domain size is accompanied by enhanced defectiveness. A further increase in EVA content up to 40 wt.% does not cause any additional significant drop in the mechanical strength of the blends.

A subsequent increase in EVA beyond 40 wt.% results in phase inversion, forming a co-continuous morphology of two independent polymer networks within the composition range of 30–60 wt.% PLA. In this exact specific range, samples exhibit the poorest mechanical properties and reduced density.

Use of AI tools declaration

The authors declare AI-assisted tools were used solely to enhance grammar, spelling, and readability. No AI tool was used for data generation, analysis, or interpretation. All intellectual and scientific contributions are the authors' original work.

Acknowledgments

The investigations were performed by means of the equipment of the common use centers of Plekhanov Russian University and Emanuel Institute of Biochemical Physics.

Author contributions

Leonid Vayshbeyn: visualization, writing—original draft, investigation; Elena Mastalygina: conceptualization, writing—review & editing, formal analysis; Bekzod Khaydarov: investigation,

resources; Aleksey Krivandin: investigation, resources, writing—review & editing; Anatoly Popov: writing—review & editing, supervision.

Conflict of interest

The authors declare no conflict of interest.

References

1. Bose A, Paul S, Mukherjee S, et al. (2026) Bio-degradable polymers through green chemistry: Advances, applications, and future perspectives. *Discov Chem* 3: 282. https://doi.org/10.1007/s44371-026-00727-0
2. Mastalygina EE, Podzorova MV, Pantyukhov PV, et al. (2024) Fibers and filaments from polylactic acid: Production features, structure, and physical–mechanical properties. *Polym Sci Ser D* 17: 181–186. https://doi.org/10.1134/S1995421223700296
3. Brovina SD, Guivan MY, Mastalygina EE, et al. (2024) Polymer materials for 3D printing (fused deposition modelling). *Polym Sci Ser D* 17: 450–454. https://doi.org/10.1134/s199542122470076x
4. Hamad K, Kaseem M, Yang HW, et al. (2015) Properties and medical applications of polylactic acid: A review. *Express Polym Lett* 9: 435–455. https://doi.org/10.3144/expresspolymlett.2015.42
5. Rasal RM, Janorkar AV, Hirt DE (2010). Poly (lactic acid) modifications. *Prog Polym Sci* 35: 338–356. https://doi.org/10.1016/j.progpolymsci.2009.12.003
6. Puthumana M, Santhana Gopala Krishnan P, Nayak SK (2020) Chemical modifications of PLA through copolymerization. *Int J Polym Anal Charact* 25: 634–648. https://doi.org/10.1080/1023666X.2020.1830650
7. Cheng Y, Deng S, Chen P, et al. (2009) Polylactic acid (PLA) synthesis and modifications: A review. *Front Chem China* 4: 259–264. https://doi.org/10.1007/s11458-009-0092-x
8. Kaliva M, Georgopoulou A, Dragatogiannis DA, et al. (2020) Biodegradable chitosan-graft-poly (l-lactide) copolymers for bone tissue engineering. *Polymers* 12: 316. https://doi.org/10.3390/polym12020316
9. Deng S, Bai H, Liu Z, et al. (2019) Toward supertough and heat-resistant stereocomplex-type polylactide/elastomer blends with impressive melt stability via *in situ* formation of graft copolymer during one-pot reactive melt blending. *Macromolecules* 52: 1718–1730. https://doi.org/10.1021/acs.macromol.8b02626
10. Olkhov AA, Alekseeva OV, Konstantinova ML, et al. (2024) Effect of glycero-(9, 10-trioxolane)-trialeate ozonide on structure and mechanical properties of ultrathin polylactide fibers produced by electrospinning. *Inorg Mater Appl Res* 15: 1023–1030. https://doi.org/10.1134/S2075113324700552
11. Ma P, Hristova-Bogaerds DG, Goossens JGP, et al. (2012) Toughening of poly (lactic acid) by ethylene-co-vinyl acetate copolymer with different vinyl acetate contents. *Eur Polym J* 48: 146–154. https://doi.org/10.1016/j.eurpolymj.2011.10.015

12. Xu P, Ma P, Hoch M, et al. (2016) Transparent blown films from poly (lactide) and poly (ethylene-co-vinyl acetate) compounds: Structure and property. *Polym Degrad Stab* 129: 328–337. https://doi.org/10.1016/j.polymdegradstab.2016.05.010
13. Kugimoto D, Kouda S, Yamaguchi M (2019) Improvement of mechanical toughness of poly (lactic acid) by addition of ethylene-vinyl acetate copolymer. *Polym Test* 80: 106021. https://doi.org/10.1016/j.polymertesting.2019.106021
14. Kugimoto D, Kouda S, Yamaguchi M (2021) Modification of poly (lactic acid) rheological properties using ethylene–vinyl acetate copolymer. *J Polymers Environ* 29: 121–129. https://doi.org/10.1007/s10924-020-01856-y
15. Karimpour-Motlagh N, Moghadam AS, Khonakdar HA, et al. (2020) A theoretical and experimental analysis of the effect of nanoclay on gas perm-selectivity of biodegradable PLA/EVA blends in the presence and absence of compatibilizer. *Macromol Mater Eng* 305: 2000433. https://doi.org/10.1002/mame.202000433
16. Ishaque N, Naseer N, Abbas MA, et al. (2022) Optimize PLA/EVA polymers blend compositional coating for next generation biodegradable drug-eluting stents. *Polymers* 14: 3547. https://doi.org/10.3390/polym14173547
17. Han DH, Choi MC, Nagappan S, et al. (2020) Ethylene vinyl acetate (EVA)/poly (lactic acid) (PLA) blends and their foams. *Mol Cryst Liq Cryst* 707: 38–45. https://doi.org/10.1080/15421406.2020.1743453
18. Tábi T (2019) The application of the synergistic effect between the crystal structure of poly (lactic acid) (PLA) and the presence of ethylene vinyl acetate copolymer (EVA) to produce highly ductile PLA/EVA blends. *J Therm Anal Calorim* 138: 1287–1297. https://doi.org/10.1007/s10973-019-08184-x
19. Romero LM, Palacio DA, Esquivel S, et al. (2024) Contact antibacterial and biocompatible polymeric, composite with copper zeolite filler and copper oxide, nanoparticles: A step towards new raw materials for the biomedical industry. *Polymer* 315: 127795. https://doi.org/10.1016/j.polymer.2024.127795
20. Unverzagt L, Dolynchuk O, Lettau O, et al. (2024) Characteristics and challenges of poly(ethylene-ico/i-vinyl acetate) solution electrospinning. *ACS Omega* 9: 18624–18633. http://doi.org/10.1021/acsomega.4c01452
21. ISO (2024) ISO 6775:2024 Plastics—Plastics identification using Raman spectrometric methods. International Organization for Standardization. Available from: https://www.iso.org/standard/82370.html.
22. ISO (2011) ISO 10640:2011 Plastics—Methodology for assessing polymer photoageing by FTIR and UV/visible spectroscopy. International Organization for Standardization. Available from: https://www.iso.org/standard/46024.html.
23. ISO (2023) ISO 11357-1:2023 Plastics—Differential scanning calorimetry (DSC)—Part 1: General principles. International Organization for Standardization. Available from: https://www.iso.org/standard/83904.html.
24. Alderton D (2021) X-ray diffraction (XRD), In: Alderton D, Elias SA, *Encyclopedia of Geology (Second Edition)*, Oxford: Academic Press, 520–531. https://doi.org/10.1016/B978-0-08-102908-4.00178-8

25. Krivandin AV, Fatkullina LD, Shatalova OV, et al. (2013) Small-angle X-ray scattering study of the incorporation of ICHPHAN antioxidant in liposomes. *Russ J Phys Chem B* 7: 338–342. https://doi.org/10.1134/S1990793113050072
26. ISO (2019) ISO 527-1:2019 Plastics—Determination of tensile properties—Part 1: General principles. International Organization for Standardization. Available from: https://www.iso.org/standard/527-1.html.
27. ISO (2022) ISO 1133-1:2022 Plastics—Determination of the melt mass-flow rate (MFR) and melt volume-flow rate (MVR) of thermoplastics—Part 1: Standard method. International Organization for Standardization. Available from: https://www.iso.org/standard/83905.html.
28. ISO (2019) ISO 1183-1:2019 Plastics—Methods for determining the density of non-cellular plastics—Part 1: Immersion method, liquid pycnometer method and titration method. International Organization for Standardization. Available from: https://www.iso.org/standard/74990.html.
29. Fekete E, Pukánszky B (2005) Effect of molecular interactions on the miscibility and structure of polymer blends. *Eur Polym J* 41: 727–736. https://doi.org/10.1016/j.eurpolymj.2004.10.038
30. Utracki LA, Wilkie CA (2014) *Polymer Blends Handbook*, 2 Eds., Dordrecht: Springer. https://doi.org/10.1007/978-94-007-6064-6
31. Moradi S, Yeganeh JK (2020) Highly toughened poly (lactic acid) (PLA) prepared through melt blending with ethylene-co-vinyl acetate (EVA) copolymer and simultaneous addition of hydrophilic silica nanoparticles and block copolymer compatibilizer. *Polym Test* 91: 106735. https://doi.org/10.1016/j.polymertesting.2020.106735
32. Cuiffo MA, Snyder J, Elliott AM, et al. (2017) Impact of the fused deposition (FDM) printing process on polylactic acid (PLA) chemistry and structure. *Appl Sci* 7: 579. https://doi.org/10.3390/app7060579
33. Hirschl C, Neumaier L, Mühleisen W, et al. (2016) In-line determination of the degree of crosslinking of ethylene vinyl acetate in PV modules by Raman spectroscopy. *Sol Energy Mater Sol Cells* 152: 10–20. https://doi.org/10.1016/j.solmat.2016.03.019
34. Kister G, Cassanas G, Vert M (1998) Effects of morphology, conformation and configuration on the IR and Raman spectra of various poly (lactic acid)s. *Polymer* 39: 267–273. https://doi.org/10.1016/S0032-3861(97)00229-2
35. Bredács M, Barretta C, Castillon LF, et al. (2021) Prediction of polyethylene density from FTIR and Raman spectroscopy using multivariate data analysis. *Polym Test* 104: 107406. https://doi.org/10.1016/j.polymertesting.2021.107406
36. Abushakhmanova ZR, Mastalygina EE, Pantyukhov PV, et al. (2024) Structure formation and interaction of polyethylene and polycaprolactone in blends. *Russ J Phys Chem A* 98: 1363–1371. https://doi.org/10.1134/S0036024424700353
37. Hemmati F, Garmabi H, Modarress H (2014) Phase behavior of polyethylene/ethylene vinyl acetate blends: Studies on miscibility window, composition dependency of interfacial interactions, and enhanced toughness. *J Plastic Film Sheeting* 31: 8–26. https://doi.org/10.1177/8756087914525962
38. Smith BC (2022) Infrared spectroscopy of polymers, VIII: Polyesters and the rule of three. *Spectroscopy* 37: 25–28. https://doi.org/10.56530/spectroscopy.ta9383e3

39. Lee HW, Insyani R, Prasetyo D, et al. (2015) Molecular weight and structural properties of biodegradable PLA synthesized with different catalysts by direct melt polycondensation. *J Eng Technol Sci* 47: 364–373. https://doi.org/10.5614/j.eng.technol.sci.2015.47.4.2
40. Smith BC (2021) The infrared spectra of polymers II: Polyethylene. *Spectroscopy* 36: 24–29. https://doi.org/10.56530/spectroscopy.xp7081p7
41. Everaert V, Aerts L, Groeninckx G (1999) Phase morphology development in immiscible PP/(PS/PPE) blends influence of the melt-viscosity ratio and blend composition. *Polymer* 40: 6627–6644. https://doi.org/10.1016/S0032-3861(99)00048-8
42. Chan CM, Feng J (1997) Mechanisms for viscosity reduction of polymer blends: Blends of fluoroelastomer and high-density polyethylene. *J Rheol* 41: 319–333. https://doi.org/10.1122/1.550805
43. Kuwahara R, Tomita R, Ogawa N, et al. (2017) Crystallization and hardening of poly (ethylene-co-vinyl acetate) mouthguards during routine use. *Sci Rep* 7: 44672. https://doi.org/10.1038/srep44672
44. Müller AJ, Ávila M, Saenz G, et al. (2014) *Crystallization of PLA-based Materials*, 1 Eds., Cambridge: Royal Chemistry Series. https://doi.org/10.1039/9781782624806-00066
45. Di Lorenzo ML, Rubino P, Immirzi B, et al. (2015) Influence of chain structure on crystal polymorphism of poly (lactic acid). Part 2. Effect of molecular mass on the crystal growth rate and semicrystalline morphology. *Colloid Polym Sci* 293: 2459–2467. https://doi.org/10.1007/s00396-015-3709-2
46. Yasuniwa M, Tsubakihara S, Sugimoto Y, et al. (2004) Thermal analysis of the double-melting behavior of poly (L-lactic acid). *J Polym Sci B Polym Phys* 42: 25–32. https://doi.org/10.1002/polb.10674
47. Wang Y, Mano JF (2005) Influence of melting conditions on the thermal behaviour of poly (l-lactic acid). *Eur Polym J* 41: 2335–2342. https://doi.org/10.1016/j.eurpolymj.2005.04.030
48. Yasuniwa M, Tsubakihara S, Iura K, et al. (2006) Crystallization behavior of poly (l-lactic acid). *Polymer* 47: 7554–7563. https://doi.org/10.1016/j.polymer.2006.08.054
49. Csézi G, Mészáros L, Tábi T (2026) Enhanced crystallinity, toughness, and heat resistance of PLA using EVA, nucleating agent, and controlled crystallization. *Polym Bull* 83: 170. https://doi.org/10.1007/s00289-025-06225-0
50. Ali AM (2022) The impact of the thermal annealing conditions on the structural properties of polylactic acid fibers. *Microsc Res Tech* 85: 875–881. https://doi.org/10.1002/jemt.23956
51. Benkraled L, Zennaki A, Zair L, et al. (2024) Effect of plasticization/annealing on thermal, dynamic mechanical, and rheological properties of poly(lactic acid). *Polymers* 16: 974. https://doi.org/10.3390/polym16070974
52. Wasanasuk K, Tashiro K (2011) Crystal structure analysis of poly(l-lactic acid) α form on the basis of the 2-dimensional wide-angle synchrotron X-ray and neutron diffraction measurements. *Macromolecules* 44: 6441–6452. https://doi.org/10.1021/ma2006624
53. Wasanasuk K, Tashiro K (2011) Crystal structure and disorder in Poly (l-lactic acid) δ form (α′ form) and the phase transition mechanism to the ordered α form. *Polymer* 52: 6097–6109. https://doi.org/10.1016/j.polymer.2011.10.046
54. Wang H, Zhang J, Tashiro K (2017) Phase transition mechanism of poly(l-lactic acid) among the α, δ, and β forms on the basis of the reinvestigated crystal structure of the β form. *Macromolecules* 50: 3285–3300. https://doi.org/10.1021/acs.macromol.7b00272

55. Serenko OA, Goncharuk GP, Obolonkova ES, et al. (2006) The brittle-ductile transition in rubber-filled polymers. *Polym Sci Ser A* 48: 302–313. https://doi.org/10.1134/S0965545X06030114
56. Agrawal P, Araújo AP, Lima JC, et al. (2019) Rheology, mechanical properties and morphology of poly (lactic acid)/ethylene vinyl acetate blends. *J Polymers Environ* 27: 1439–1448. https://doi.org/10.1007/s10924-019-01445-8
57. Hu X, Jiang Z, Narayanan S, et al. (2006) Observation of a low-viscosity interface between immiscible polymer layers. *Phys Rev E* 74: 010602. https://doi.org/10.1103/PhysRevE.74.010602
58. Steinmann S, Gronski W, Friedrich C (2001) Cocontinuous polymer blends: Influence of viscosity and elasticity ratios of the constituent polymers on phase inversion. *Polymer* 42: 6619–6629. https://doi.org/10.1016/S0032-3861(01)00100-8
59. Aggarwal N, Sarkar K (2008) Effects of matrix viscoelasticity on viscous and viscoelastic drop deformation in a shear flow. *J Fluid Mech* 601: 63–84. https://doi.org/10.1017/S0022112008000451



AIMS Press

© 2026 the Author(s), licensee AIMS Press. This is an open access article distributed under the terms of the Creative Commons Attribution License (https://creativecommons.org/licenses/by/4.0)